Chapter 30

Internal Tilt-Compensated Coma-Free Decenter of the AXAF mirrors

Terrance J. Gaetz

This chapter discusses the investigation and analysis of one of the major "minor mysteries" encountered during Phase 1 testing at XRCF. The first two sections (§30.1 and §30.2) provide a brief description of the investigation which led to the discovery of the "tilt-compensated" (*i.e.*, *coma-free*) decenters between the P and H optics in the HRMA. Although the decenter was first detected in quadrant flux balance measurements, detailed off-axis X-ray images led to a much more powerful approach to determining the decenter values. The detailed morphology of the X-ray images is discussed in §30.3. The measurements of the tilt-compensated decenters are described in §30.4. Finally, in §30.5 some suggestions are made for future investigation.

30.1 Quadrant Shutter Flux Balance

During the attempts to assess the relation between the HRMA optical axis and the FOA, a series of quad-shutter flux balance experiments were performed. These tests were part of an attempt to measure the misalignment of the HRMA optical axis relative to the Facility Optical Axis (FOA) by the variation in the amount of flux detected through individual mirror quadrants. For example, as the HRMA pitch is changed, one would expect the relationship between the fluxes from the Top and Bottom quadrants to change. The "2nd Floor" scientists at XRCF noted anomalies which were difficult to explain: an asymmetry of 6 or 7% between the Shell 6 top and bottom shutter fluxes (and correspondingly smaller asymmetries for the larger shells) even though other evidence suggested that HRMA axis alignment to the FOA in pitch was really rather close.

Various suggestions were considered. The effects of vignetting by various baffles and obstructions were investigated, but in each case the required decenters were too large to be plausible (*e.g.*, decenters of the precollimator by several millimeters), the size of the effect was too small, or the effect did not fit the observed trends very well. Tests at ring focus exonerated the shutter assembly itself (see Chapter 25). Finally it was suggested by that an internal relative decenter between the P and H optic might explain the anomalies. Preliminary raytrace investigations showed that a pure decenter of several hundred μm could affect the flux balance in the way observed. Because such large decenters would have been immediately noticed in the optical coma measurements (Chapter 27), it was postulated that a coma-free combination of decenter plus tilt ("tilt-compensated decenter") was responsible. In the case of an H optic, this motion is a rigid-body rotation of the H optic

about its far focus; the coma from the tilt component of the motion exactly cancels the coma produced by the decenter component. Further raytraces showed that the decenter component of the tilt-compensated decenter accounted for most of the flux balance anomaly; although the tilt compensation is needed to account for the observed coma, the tilt compensation modified the flux balance discrepencies by $\lesssim$10%.)

C. Atkinson (EKC) reviewed the assembly procedure and came up with a scenario whereby an initial decenter could have been introduced between P6 and the optical axis and which would naturally lead to each of the mirror pairs having approximately the same tilt-compensated decenters; tolerances are such that a relative decenter of a few hundred μm are possible.

Noise and systematic errors made it difficult to obtain good values of the decenters from the flux balance differences alone.

30.2 Off-Axis X-ray Images

Off-axis HSI images for the whole HRMA were taken at a number of off-axis angles and energies (see Table 30.1). These off-axis images showed a peculiar pincushion-like cuspy feature in the core and this proved to be the breakthrough needed for understanding the P to H decenters. Preliminary raytrace studies confirmed that a P to H decenter of several hundred μm could generate pincushion-like cusps in off-axis images qualitatively similar to those observed. The off-axis images established tilt-compensated decenter as the most likely explanation for the flux balance results; any explanation in terms of obscuration or vignetting would fail to account for the distinctive characteristic features in the off-axis X-ray images.

Considerable effort was expended in attempting to deduce the optic decenters from the available full-HRMA images at different energies; T. Gaetz (SAO) determined that two mirror pairs (at least) exhibited a tilt-compensated decenter, probably of about the same magnitude and direction, but the complexity of four overlapping images made it very difficult to make further progress. (Even the identification between pincushion and responsible mirror shell was problematic; some of the tentative identifications proved to be incorrect.)

In order to diagnose the P to H decenters which seemed to be implied by the quadrant flux balance data and the full-HRMA off-axis images, a series of off-axis images for individual mirror pairs was requested and obtained. These images were all at Al-Kα (see Table 30.2) and are plotted in Figures 30.1, 30.2, and 30.3.

Systematic raytrace investigations were undertaken to understand the effect of tilt-compensated decenter on off-axis images (T.Gaetz, SAO); as a result of these studies, a scheme was developed for deriving the decenter parameters based on detailed measurements of image features. The results of these studies and the resulting tilt-compensated decenter parameters as assessed from the X-ray images are described below.

30.3 Morphology of the Off-axis X-ray Images

The off-axis images taken at XRCF show two distinctive features: a pair of overlapping large, approximately oval lobes, and a small pincushion-like caustic in the core. This section discusses the morphology of these features and their dependence on decenter magnitude and direction relative to the off-axis source direction.

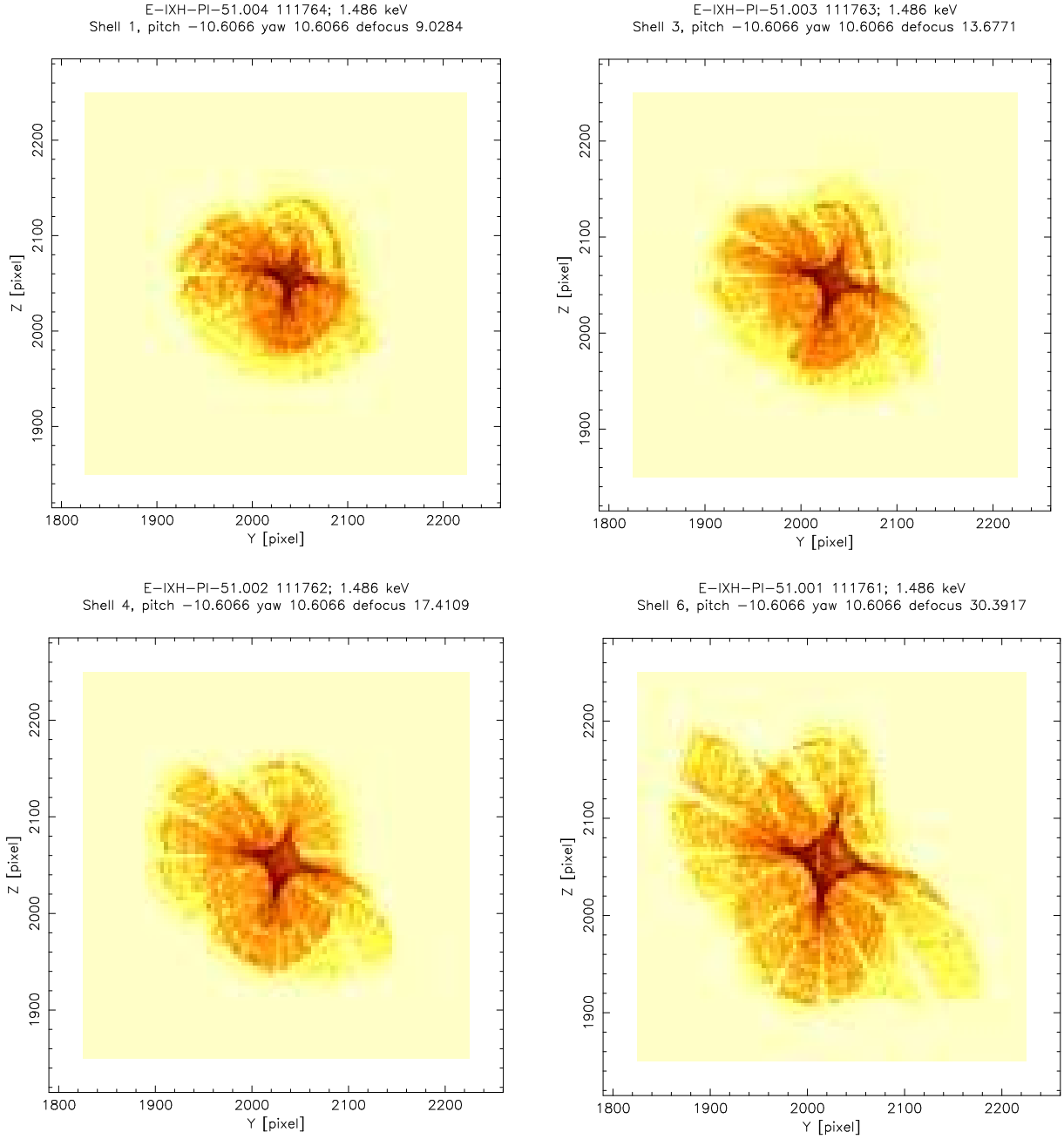

Figure 30.1: Off-axis images for individual shells; pitch = $-10.61'$, yaw = $10.61'$. Pixel width 6.43 μm; binned to 4×4 pixels. Two large overlapping lobes and a dense central pincushion can be seen; the light lanes are shadows of the CAP struts. The concentric ridges in the large lobes result from low-frequency surface errors on the mirrors. (X-ray data; logarithmic stretch)

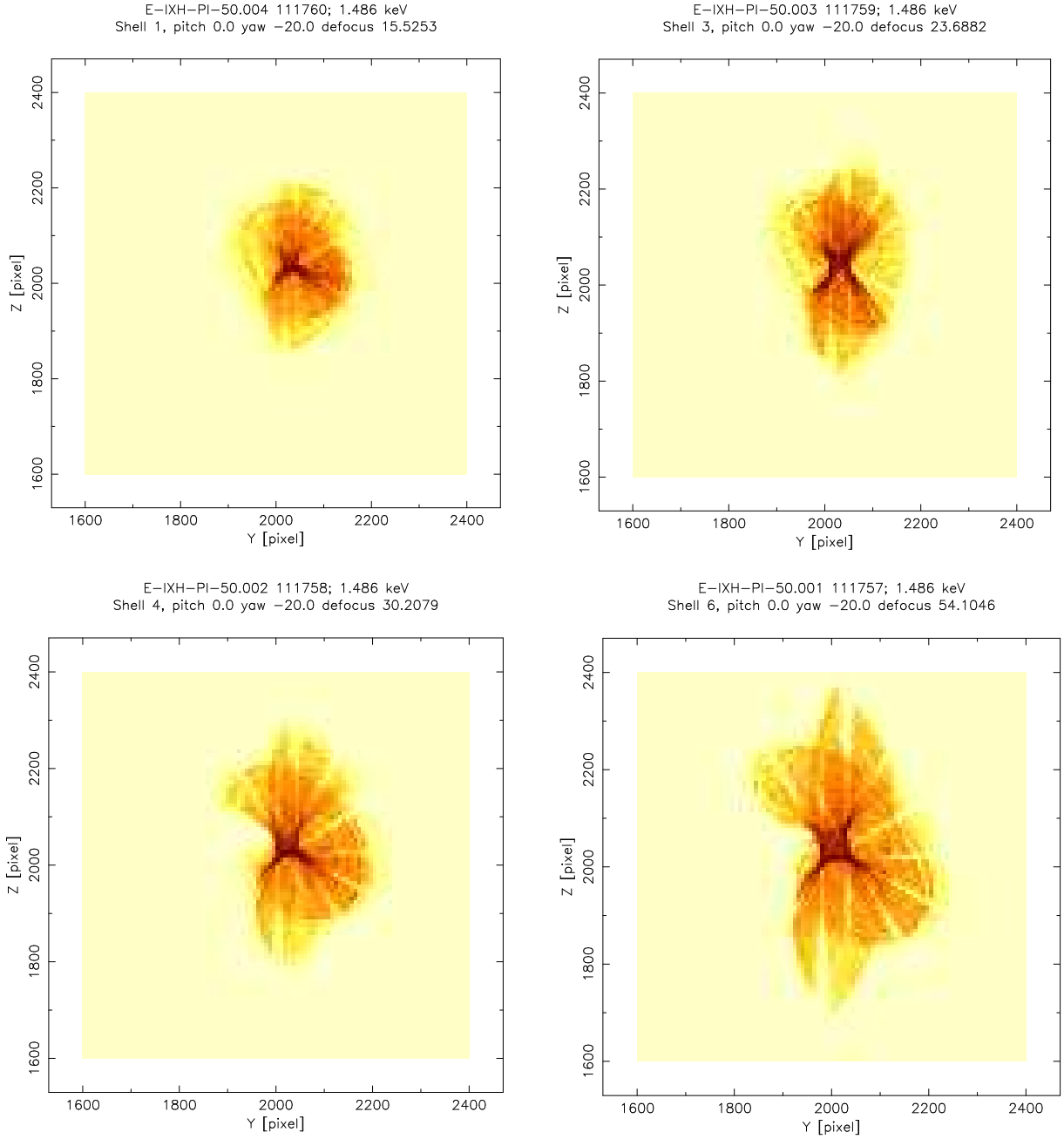

Figure 30.2: Off-axis images for individual shells; pitch = $0'$, yaw = $-20'$. Pixel width $6.43\,\mu$m; binned to 8×8 pixels. Two large overlapping lobes and a dense central pincushion can be seen; the light lanes are shadows of the CAP struts. The concentric ridges in the large lobes result from low-frequency surface errors on the mirrors. (X-ray data; logarithmic stretch)

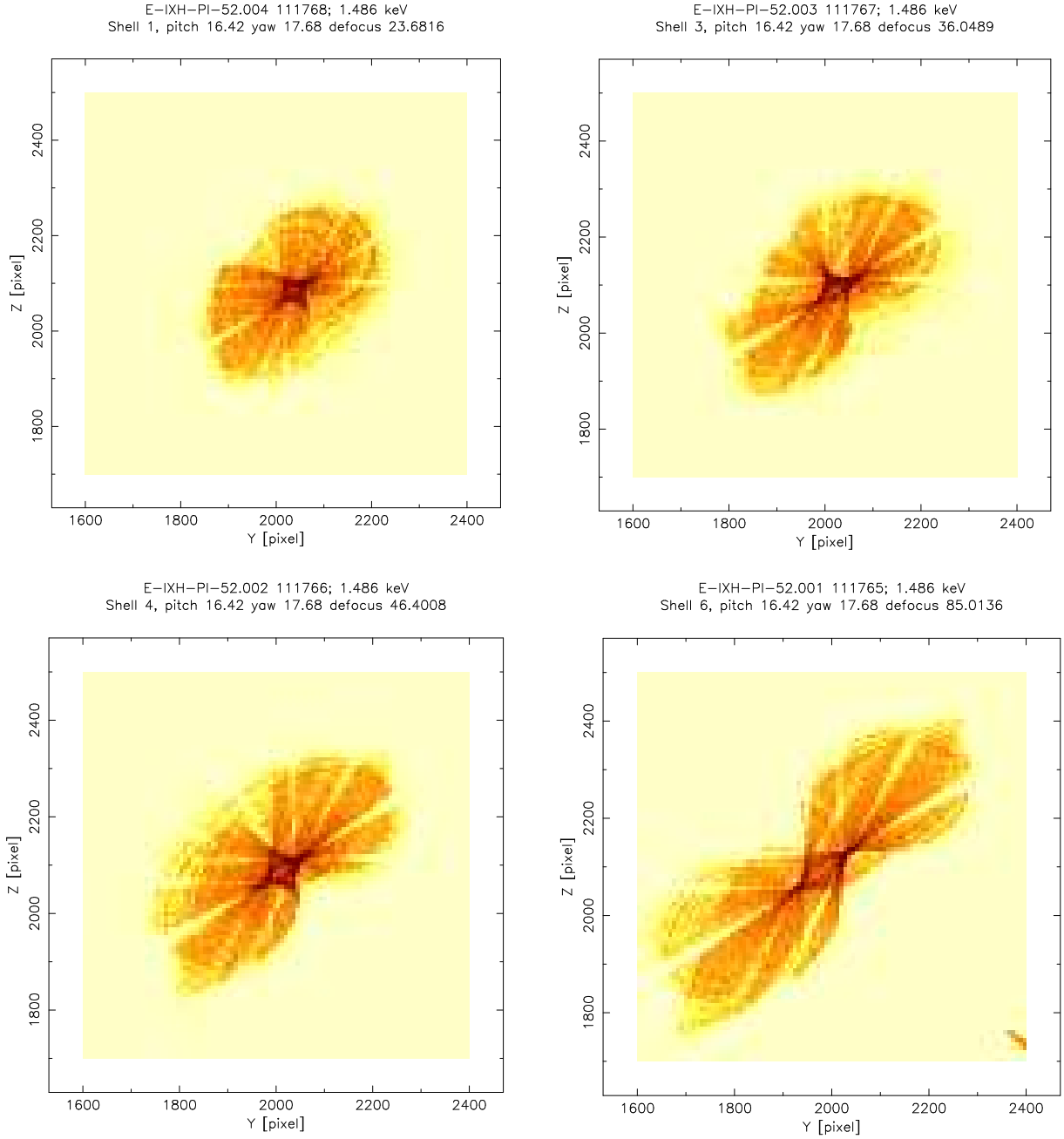

Figure 30.3: Off-axis images for individual shells; pitch = 16.42′, yaw = 17.68′. Pixel width 6.43 μm; binned to 8×8 pixels. Two large overlapping lobes and a dense central pincushion can be seen; the light lanes are shadows of the CAP struts. The concentric ridges in the large lobes result from low-frequency surface errors on the mirrors. (X-ray data; logarithmic stretch)

Table 30.1: Phase 1 Off-Axis Images (Full HRMA)

TRW ID	RunID	Energy	Shell	pitch	yaw	defocus
E-IXH-PI-6.001	110594	0.277	HRMA	−3.54	3.54	1.4384
E-IXH-PI-7.002	110639	0.277	HRMA	0	−10	5.6211
E-IXH-PI-6.003	110668	0.277	HRMA	−10.61	10.61	12.1095
E-IXH-PI-7.004	110669	0.277	HRMA	0	−20	20.6847
E-IXH-PI-6.005	110700	0.277	HRMA	−17.68	17.68	31.1065
E-IXH-PI-6.006	110701	0.277	HRMA	−21.21	21.21	44.7368
E-IXH-PI-12.004	110887	6.4	HRMA	0	−20	20.6847
E-IXH-PI-12.002	110888	6.4	HRMA	0	−10	5.6211
E-IXH-PI-11.001	110889	6.4	HRMA	−3.54	3.54	1.4384
E-IXH-PI-11.003	110890	6.4	HRMA	−10.61	10.61	12.1095
E-IXH-PI-11.005	110892	6.4	HRMA	−17.68	17.68	31.1065
E-IXH-PI-11.006	110893	6.4	HRMA	−21.21	21.21	44.7368
E-IXH-PI-22.004	111084	4.51	HRMA	0	−20	20.6847
E-IXH-PI-22.002	111085	4.51	HRMA	0	−10	5.6211
E-IXH-PI-21.001	111086	4.51	HRMA	−3.54	3.54	1.4384
E-IXH-PI-21.003	111087	4.51	HRMA	−10.61	10.61	12.1095
E-IXH-PI-21.005	111088	4.51	HRMA	−17.68	17.68	31.1065
E-IXH-PI-21.006	111089	4.51	HRMA	−21.21	21.21	44.7368

30.3.1 Off-Axis Images: Large Lobes

The off-axis images show two large approximately oval lobes; these are a facility effect resulting from the spherical aberration which is introduced by the finite source distance at XRCF. Symmetry considerations indicate that for an ideal perfectly aligned telescope, these lobes should be symmetric about a line containing the off-axis image and the optical axis. The observed large lobes are asymmetric and also tilted relative to each other; this is a consequence of the tilt-compensated decenter within the mirror pair. The lighter swaths through the image result from shadowing by support struts, predominantly those in the Central Aperture Plate.

The approximately concentric ripples in the large lobes result from the low-order mirror surface errors; these are also caustics, analogous to the pattern of bright lines on the bottom of a swimming pool caused by the ripples on the water surface. In this case they result from axial ripples on the mirror surface. The agreement between the location and shape of the ripples in the X-ray data as compared to the raytraces is an indication of the fidelity of the low-order mirror maps used in the raytrace. The ripples are more noticeable in the Shell 1 images; Figure 30.7 shows them at a different contrast setting.

The relative balance between the sizes of the lobes is sensitive to the axial position of the detector; at the best off-axis focus for the mirror pair, these lobes are comparable in size. The relative shape and orientation of the lobes depends on the direction of the decenter relative to the direction of the off-axis source (working in HRMA-centered coordinates). In addition to the offsets in the large lobes, a relative P to H decenter produces a pincushion-shaped caustic at best (off-axis)

Table 30.2: Phase 1 Off-Axis Images (Individual Shell)

TRW ID	RunID	Energy	Shell	pitch	yaw	defocus
E-IXH-PI-50.001	111757	1.486	6	0	−20	54.1046
E-IXH-PI-50.002	111758	1.486	4	0	−20	30.2079
E-IXH-PI-50.003	111759	1.486	3	0	−20	23.6882
E-IXH-PI-50.004	111760	1.486	1	0	−20	15.5253
E-IXH-PI-51.001	111761	1.486	6	−10.61	10.61	30.3917
E-IXH-PI-51.002	111762	1.486	4	−10.61	10.61	17.4109
E-IXH-PI-51.003	111763	1.486	3	−10.61	10.61	13.6771
E-IXH-PI-51.004	111764	1.486	1	−10.61	10.61	9.0284
E-IXH-PI-52.001	111765	1.486	6	16.42	17.68	85.0136
E-IXH-PI-52.002	111766	1.486	4	16.42	17.68	46.4008
E-IXH-PI-52.003	111767	1.486	3	16.42	17.68	36.0489
E-IXH-PI-52.004	111768	1.486	1	16.42	17.68	23.6816

focus; this is discussed further in §30.3.2.

Some of the XRCF single-shell off-axis images show obvious indentations in the large lobes. In some cases (e.g., Shells 3 and 4 at pitch $= 0', \text{yaw} = -20'$, Shells 1 and 3 at pitch $= 16.42', \text{yaw} = 17.68'$) this appears to be a result of vignetting by the shutter assembly; preliminary raytraces show that a shutter assembly decenter of about 2 mm appears to be consistent with these results. In other cases the indentations arise from the morphology of the off-axis images: Shells 1 and 6 at pitch $= 0', \text{yaw} = -20'$ appears to be consistent with no additional vignetting by the shutter assembly.

A raytrace experiment was performed in which the relative direction between the off-axis source and the decenter direction was systematically varied. (The pitch and yaw of the shell were assumed fixed and the decenter direction varied.) The results are shown in Figure 30.4; a close-up of the pincushion core is shown in Figure 30.5. Note that the smaller of the large lobes and the orientation of the cuspy pincushion rotate oppositely to the change in decenter direction and at approximately half the rate that the decenter varies. The size of the pincushion also varies somewhat with relative angle between off-axis source direction and P to H mirror decenter direction. Note that the lobes and the pincushion core both show the expected bilateral symmetry when the decenter direction and the off-axis direction are parallel ($\phi = 0°$ and $\phi = 180°$.)

30.3.2 Off-Axis Images: Pincushion Caustics

The pincushion caustics are also a consequence of the tilt-compensated decenter in the optics. Raytrace studies show that the dimension of the pincushion scales inversely with the mirror pair nodal radius. The pincushion gets larger as the magnitude of the off-axis angle increases (for constant tilt-compensated decenter) and also gets larger as the magnitude of the tilt-compensated decenter increases (for constant source off-axis angle). For fixed magnitude of off-axis angle and tilt-compensated decenter, the pincushion size and the orientation of the axes of the pincushion

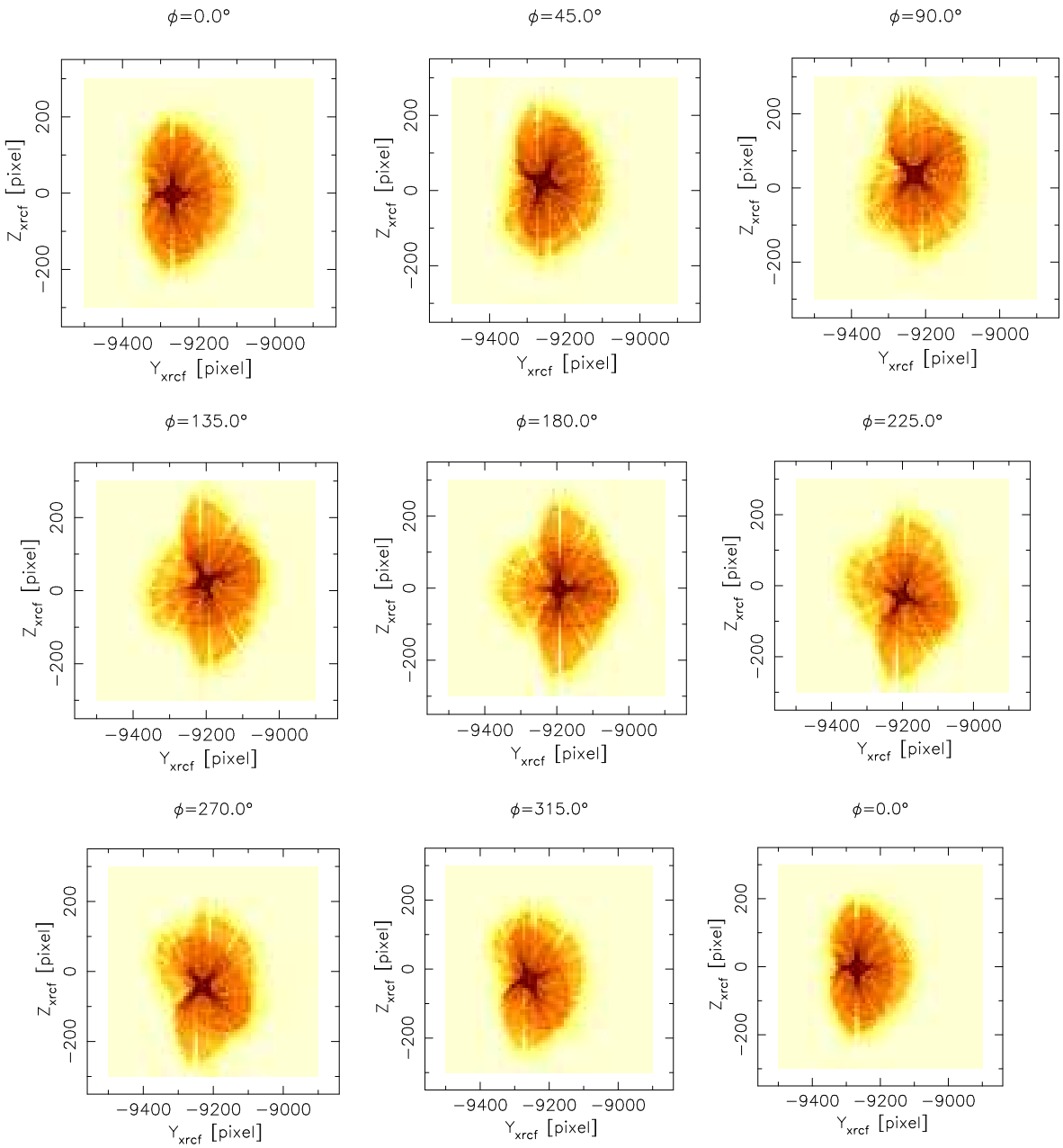

Figure 30.4: Variation of off-axis image with angle between source and decenter direction. Shell 3, pitch = 16.42′, yaw = 17.68′. Pixel width 6.43 μm; binned to 8×8 pixels. (Raytrace data; logarithmic stretch)

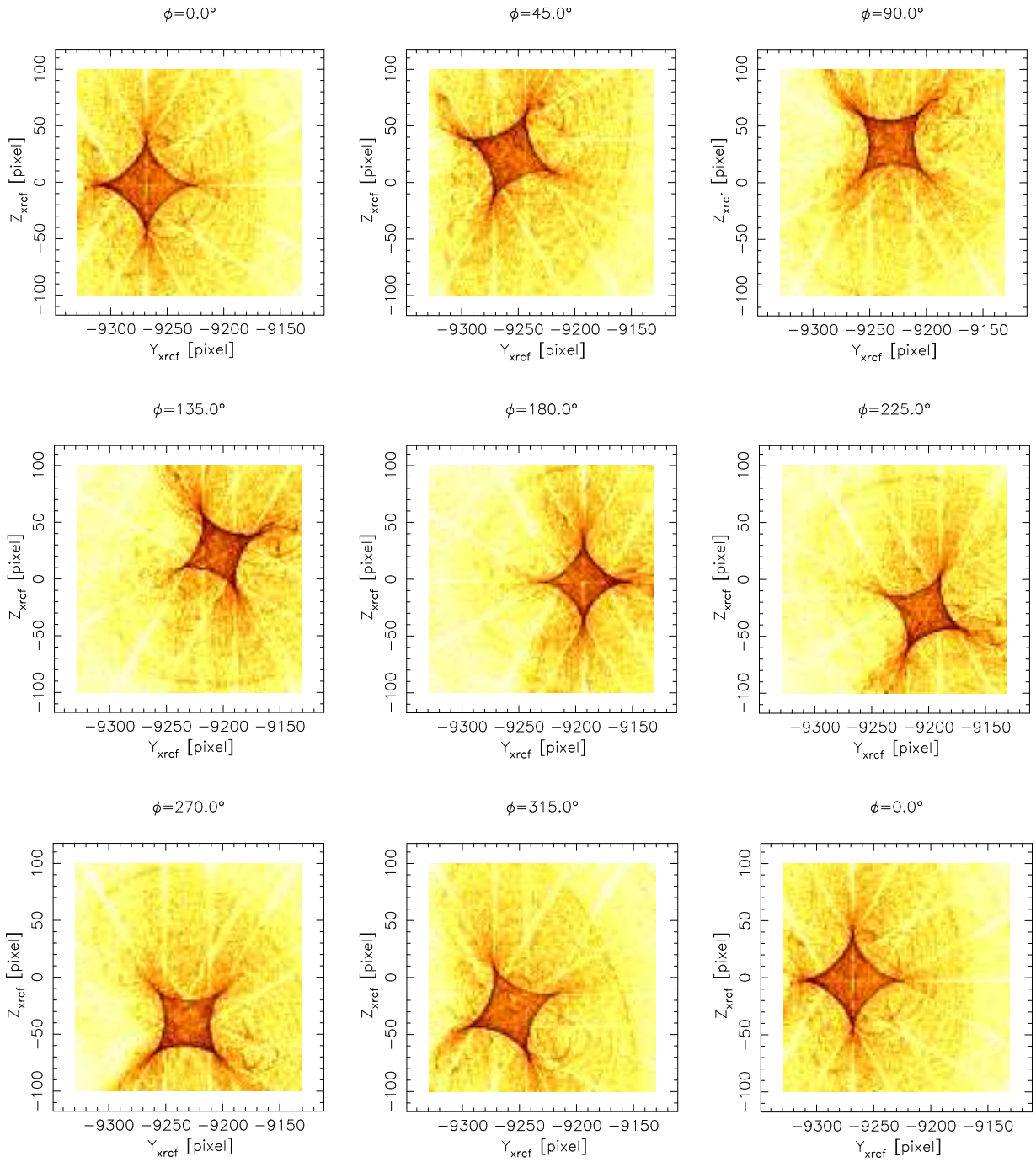

Figure 30.5: Variation of off-axis image with angle between source and decenter direction. Shell 3, pitch = 16.42′, yaw = 17.68′. Pixel width 6.43 μm; binned to 1×1 pixels. (Raytrace data; logarithmic stretch)

vary with relative angle between off-axis direction and the decenter direction. Symmetry considerations suggest that the pincushion should show full bilateral symmetry about the decenter direction when the decenter direction is parallel or anti-parallel to the off-axis direction, and this is seen in Figure 30.5 ($\phi = 0^\circ$ and $\phi = 180^\circ$ cases, where ϕ is the angle between the decenter direction and the projection onto the focal plane of the off-axis source direction); the corners of the pillbox are aligned with the decenter direction. Closer scrutiny of Figure 30.5 shows that the pincushion size varies systematically with angle between decenter direction (at fixed decenter magnitude) and (fixed) off-axis direction. The pincushion orientation changes by 90° as the ϕ changes by 180° so the pincushion rotates about half as rapidly as ϕ varies. Detailed measurements show that the factor of 1/2 is only approximate, but by symmetry, the pincushion rotation between $\phi = 0^\circ$ and $\phi = 180^\circ$ must be exactly 90° in the limit of otherwise ideal optics.

Raytracing also shows that the size and orientation of the pincushion is insensitive to the axial location of the detector; the basic structure of the pincushion is the same even with focal errors as large as several mm (though differences become readily apparent if the image is sufficiently out of focus that the pincushion unravels).

30.4 Measuring the Tilt-Compensated Decenter

Raytrace studies revealed an important feature of the tilt-compensated decenters: for constant off-axis angle and in the neighborhood of a given decenter value, the variation of the *pincushion size* with *decenter magnitude* and the variation of *pincushion orientation* with *decenter direction* are relatively uncoupled from each other. This means that once an initial estimate of the decenter parameters is obtained, the decenter magnitude and direction can be refined by using the sensitivities of pincushion size and orientation to decenter magnitude and direction to refine the estimate.

The above procedure was carried out for the single-shell pitch = $0'$, yaw = $-20'$ measurements. The approximate direction of the decenter was be assessed from the morphology of the large lobes; this also removes the $\pi/2$ angular ambiguity in the pincushion orientation (see Figure 30.4). Raytraces were used to provide an initial estimate for the magnitude and direction; the same initial values were assumed for all four shells. The relative sizes of the large lobes do depend sensitively on focal position and serve as an additional check that the images were taken at very nearly the best off-axis focus for the individual shell; examination of the X-ray data indicates that the individual shell images were taken near best focus.

The decenter magnitude and direction can be determined by measuring the pincushions in the X-ray data and simulation (on an expanded scale to make measurement easier). Figure 30.9 shows and expanded view of the the pincushion cores in the pitch= $0'$, yaw= $20'$ images, and Figure 30.10 shows the equivalent images based on raytraces using the mirror rigid-body model obtained in Chapter 27.

Figure 30.6 shows the measurement schematically. The width, w, of the pincushion along a slice through the narrow portion of the pincushion (midway up the box) was measured. In addition, the angle, θ between the Y axis and a line connecting opposing corners (at $\sim +45^\circ$) was measured. These metrics were compared with those in raytraced images. Once reasonably good agreement was obtained, a raytrace study established the sensitivity of box width w to decenter magnitude and also the sensitivity of box orientation θ to decenter direction; it was found that for Shell 6 the pincushion width w varied with decenter magnitude as 123 pixels mm^{-1} of decenter (1 pixel= 6.43 μm); the sensitivity scales inversely with the mirror nodal radius. (Note that the sensitivities may depend on the approximate magnitude of the tilt-compensated decenter and its direction relative to the off-axis source direction.)

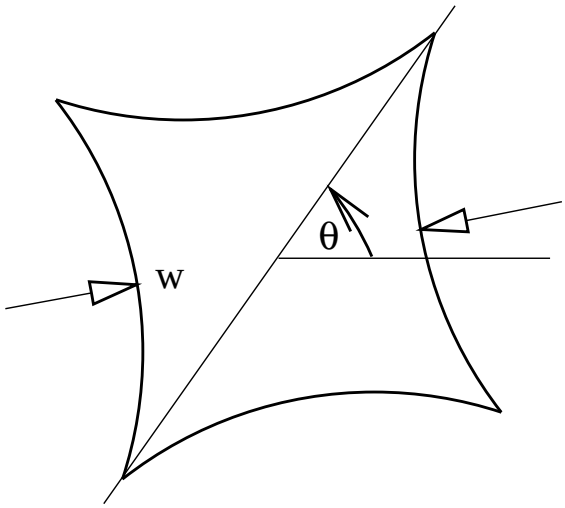

Figure 30.6: Schematic diagram of pincushion measurement. The width, w is measured across the narrow part of the pincushion. The orientation, θ, is measured using the diagonal of the pincushion.

As an illustration of the procedure, consider Figures 30.7and30.8 (Shell 1; pitch= $0'$, yaw= $-20'$). In Figure 30.7 a raytrace using the current best estimate for Shell 1 tilt-compensated decenter (upper left panel) is compared to the X-ray image (lower right panel). The effects of increasing (decreasing) the tilt-compensated decenter by 0.1 mm is shown in the lower left (upper right) panel; the change in pincushion size is clearly visible. Similarly, in Figure 30.7 the current best estimate for Shell 1 coma-free decenter+tilt (upper left panel) is compared to the X-ray image (lower right panel). The decenter is direction changed by -24° (upper right) or $+24^\circ$ (lower left); note the change in pincushion orientation. In this case it is also possible to see a darker bar across the pincushion at about 120° from about halfway across the bottom of the box; the position of this bar changes with pincushion orientation, and the agreement in bar position is quite good between the X-ray data and the current best raytrace model. (This bar is even more clearly visible in the upper left panels of Figures 30.9and30.10; a similar feature is seen in the upper right panel of Figure 30.10, but vignetting by the shutter assembly obscures that portion of the image in the corresponding X-ray data (upper right panel of Figure 30.9).)

Note that the X-ray image cores and the raytrace image cores differ in detail for at least two reasons: angle-dependent sensitivity of the HSI detector and vignetting by the quadrant shutter assembly; for example, note the vignetting evident in the bottom of the pincushion for Shell 3 and the top of the pincushion for Shell 4 in Figure 30.9. Nevertheless, the diagnostic features (pincushion size and orientation) are visible clearly enough to allow a good determination of decenter direction and magnitude. Where visible, agreement in the pincushion substructure between the X-ray data and the raytraces provides further support for the accuracy of the tilt-compensated decenter values.

The estimated relative decenters of the H mirrors relative to their mating P mirrors are given in Table 30.3. Note that these decenters are given in `SAOsac` raytrace coordinates (see Chapter B);

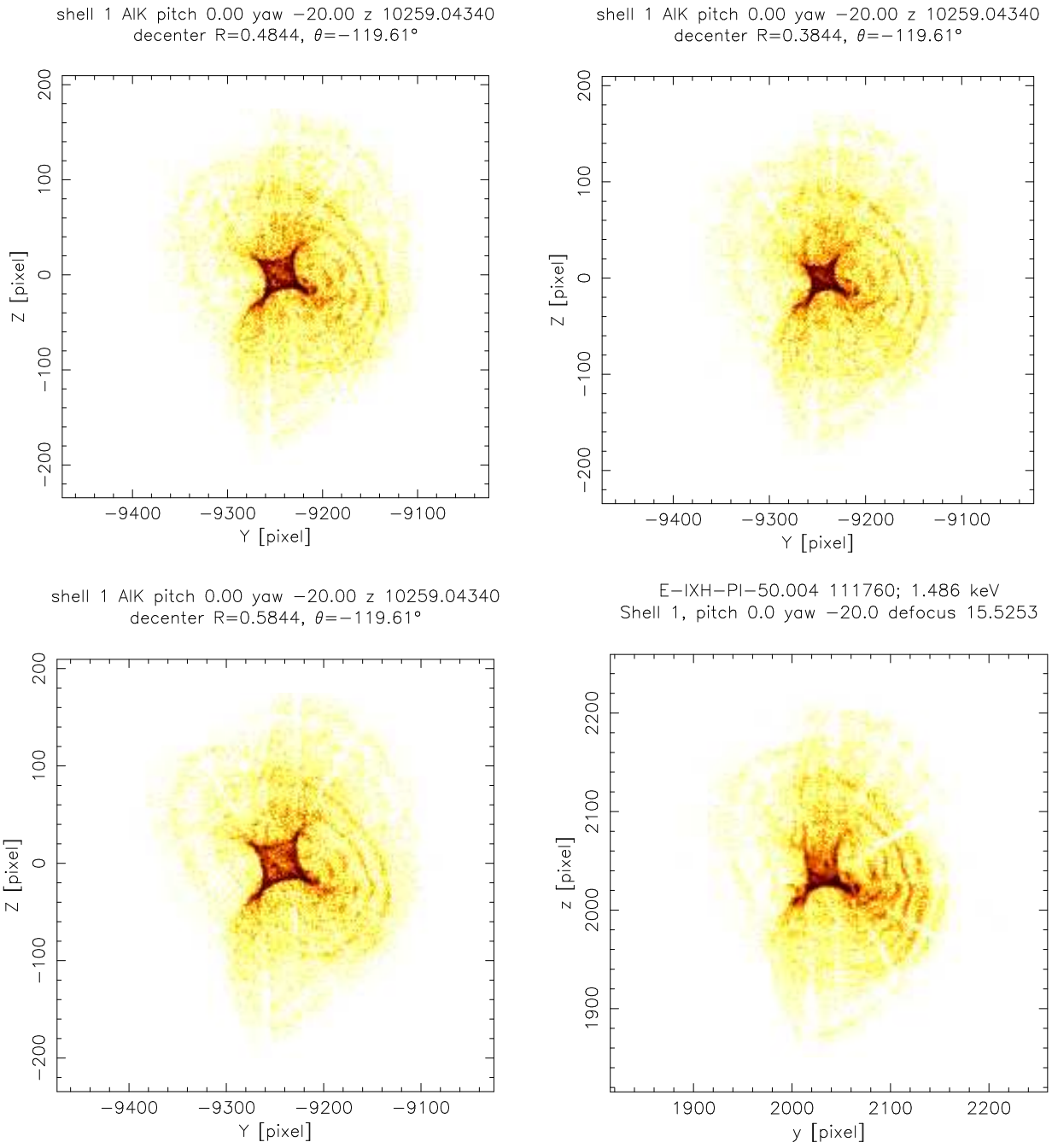

Figure 30.7: Off-axis images (Shell 1; pitch = 0′, yaw = −20′). Top left: Current raytrace model. Top right: decenter magnitude $\Delta R_0 - 0.1$ mm. Bottom left: decenter magnitude $\Delta R_0 + 0.1$ mm. Bottom right: HSI image (X-ray data) (to same scale). Pixel width 6.43 μm; binned to 2×2 pixels. Logarithmic stretch.

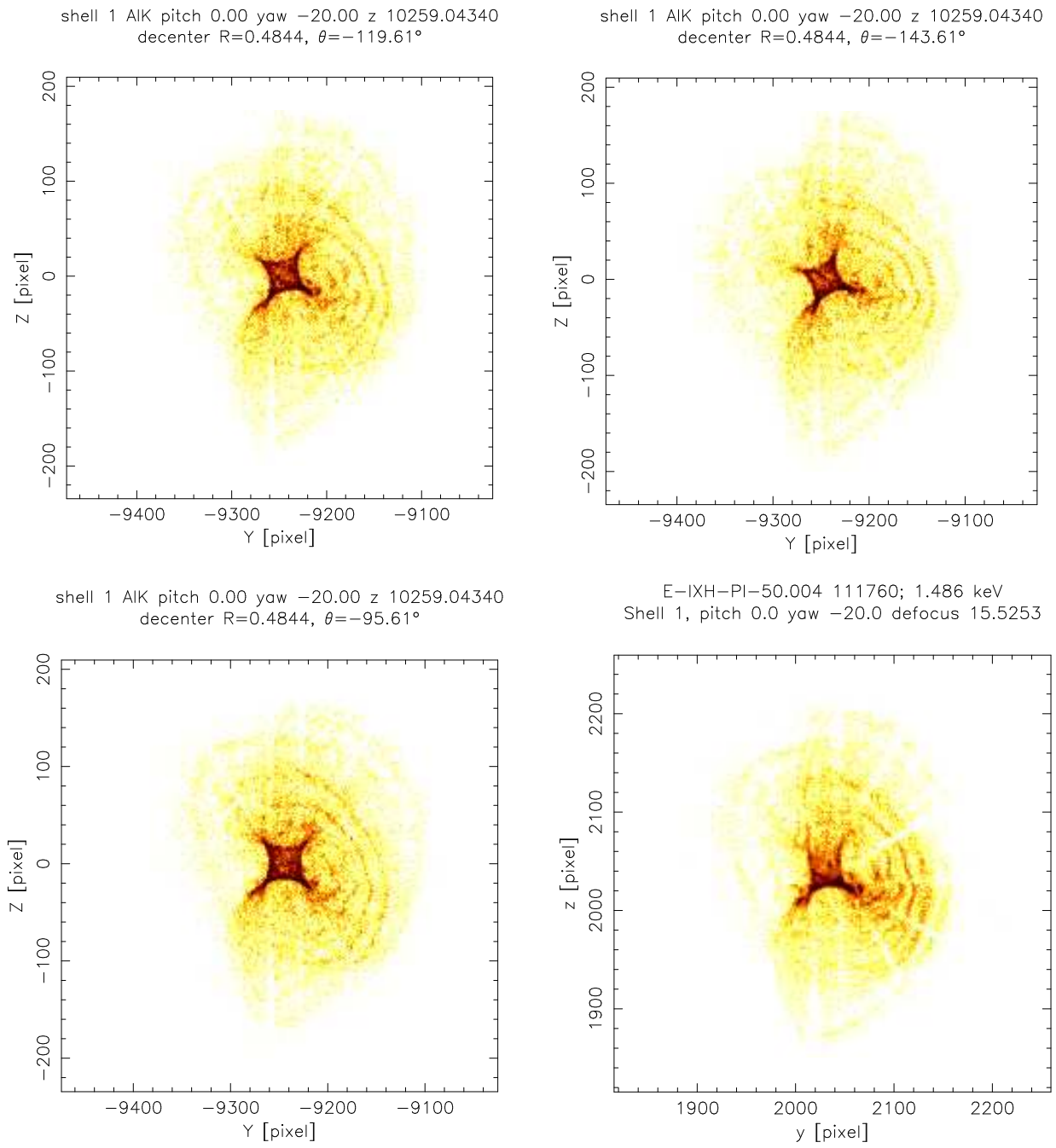

Figure 30.8: Off-axis images (Shell 1; pitch = 0′, yaw = −20′). Top left: Current raytrace model. Top right: decenter direction $\Delta\phi_0 - 24°$. Bottom left: decenter direction $\Delta\phi_0 + 24°$. Bottom right: HSI image (X-ray data) (to same scale). Pixel width 6.43 μm; binned to 2×2 pixels. Logarithmic stretch.

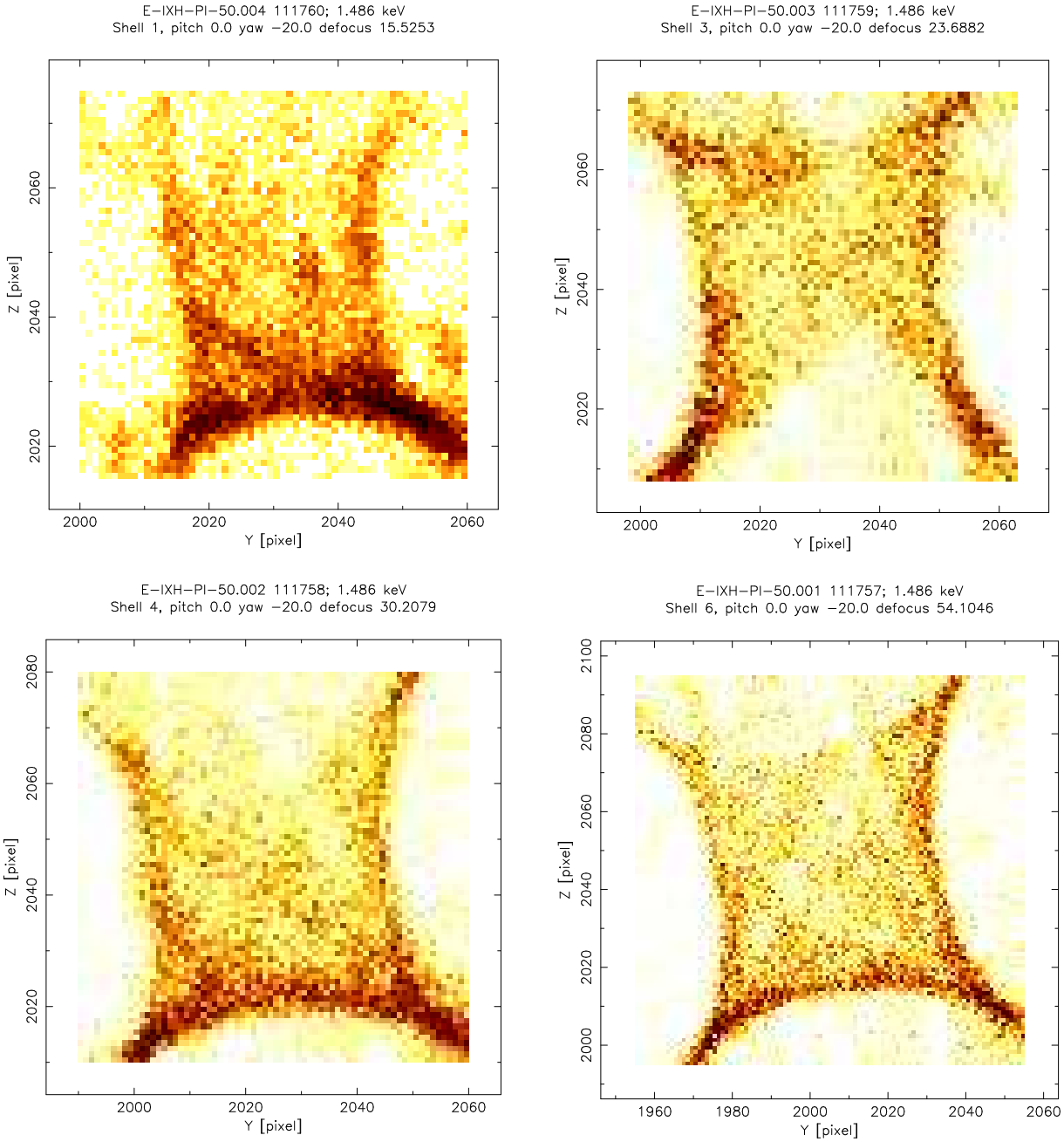

Figure 30.9: Core pincushions of off-axis images for individual shells; pitch = 0′, yaw = −20′. Pixel width 6.43 μm; binned to 1 × 1 pixels. (X-ray data; logarithmic stretch)

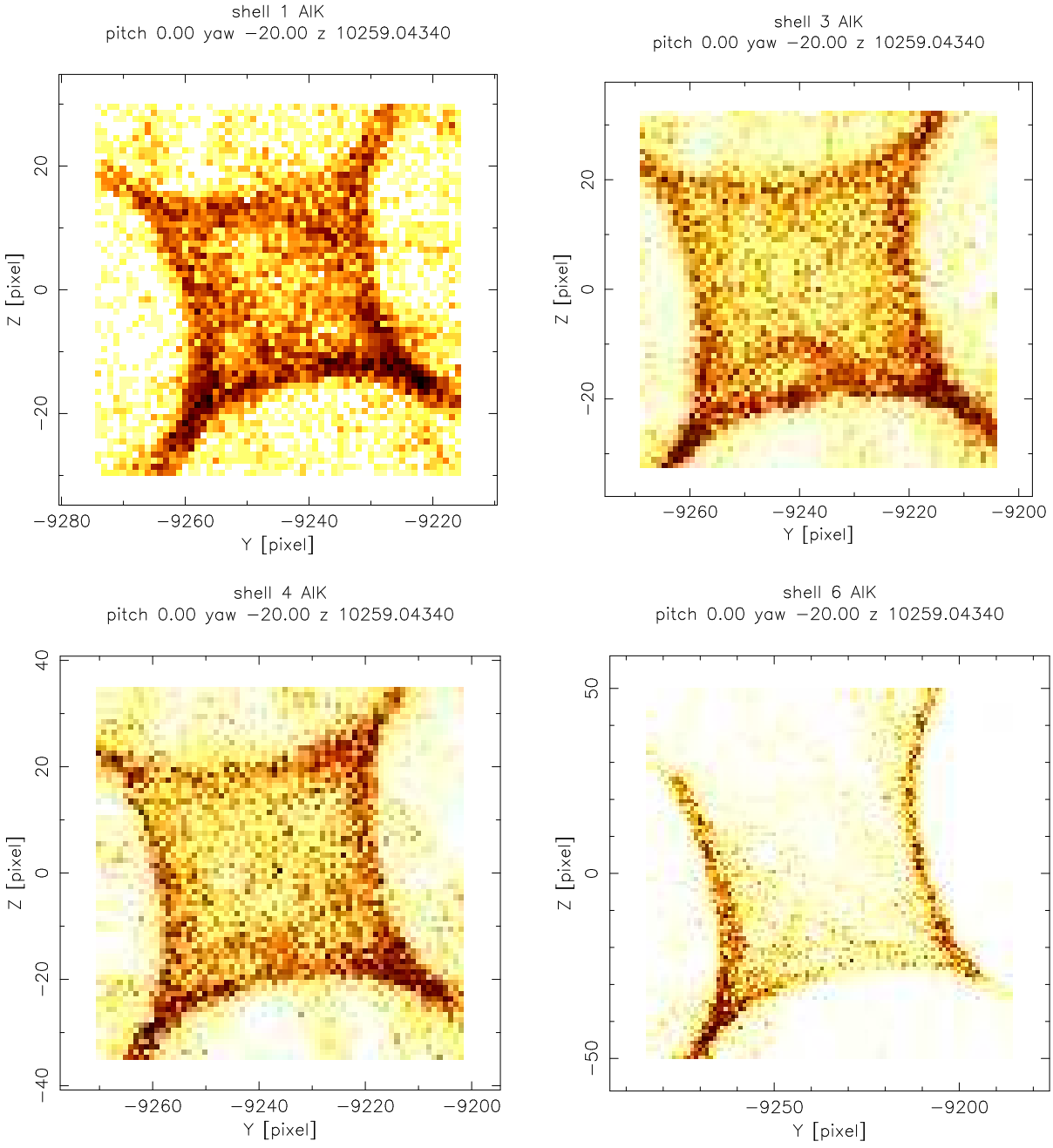

Figure 30.10: Core pincushions of off-axis images for individual shells based on current SAO raytrace model; pitch = $0'$, yaw = $-20'$. Pixel width 6.43 μm; binned to 1×1 pixels. (Raytraced; logarithmic stretch)

Table 30.3: Measured Tilt-Compensated Decenters

	decenter†		decenter†	
mirror	magnitude (mm)	angle (deg)	Δx_0 (mm)	Δy_0 (mm)
h1	0.4844	−119.61	−0.2393	−0.4211
h3	0.5077	−109.61	−0.1704	−0.4782
h4	0.4562	−111.90	−0.1702	−0.4233
h6	0.4736	−114.42	−0.1958	−0.4312

†coma from decenter cancelled by compensating tilt

angle is measured from the `SAOsac` raytrace $+X$ axis with $+Y$ at $+90°$ (see Figure B.1);

$$X_{SAOsac} = -Y_{XRCF} \tag{30.1}$$
$$Y_{SAOsac} = +Z_{XRCF} \tag{30.2}$$
$$Z_{SAOsac} = -X_{XRCF} \tag{30.3}$$
$$\tag{30.4}$$

Note that the actual body-centered decenter and tilt for each optic must also be consistent with optical measurements at EKC at the end of HRMA buildup. The construction of the mirror rigid-body database (based on the above tilt-compensated decenter and the X-ray and optical measurements of the alignment) is discussed in Chapter 27; the current mirror database is `/proj/axaf/simul/databases/mirror/EKCHDOS06.rdb`.

The current HRMA model (`trace-shell4` configuration file `xrcf_SAO1G+HDOS_HDOS-scat-970220_03`) was raytraced for each mirror pair and off-axis angle combination as listed in Table 30.2. The raytraces accumulated a total ray weight of about 100000 per image (comparable to the number of events in the X-ray images). The raytrace fractional weights were converted statistically into unit weights (`mxwldmn`) and blurred to the HSI resolution (`mcp` using the `/proj/axaf/simul/databases/detectors/hsi.par` specification file. The images *do not*, however, incorporate the angle-dependent HSI detector quantum efficiency, nor do they include the vignetting introduced by the quadrant shutter assembly at these large off-axis angles. The raytraces of the HRMA model are plotted in Figures 30.11, 30.12, and 30.13; these can be compared with the X-ray images in Figures 30.1, 30.2, and 30.3.

30.5 Future Directions

This chapter represents a preliminary attempt at extracting the tilt-compensated H to P decenters from the X-ray data. It is thought that the decenters are accurate to better than 10%. The current estimate is based on single-shell data at a single off-axis angle (pitch = $0'$, yaw = $-20'$). Single-shell off-axis X-ray images were obtained in two other directions; inspection of the raytrace data in Figures 30.11and30.13 compared to the X-ray data in Figures 30.1and30.3 shows good qualitative agreement. (Some of the detailed differences between the images are caused by vignetting by the quad shutter assembly at these large off-axis angles.) The single-shell data taken at the other two off-axis angles can be used to provide additional estimates of the tilt-compensated decenters;

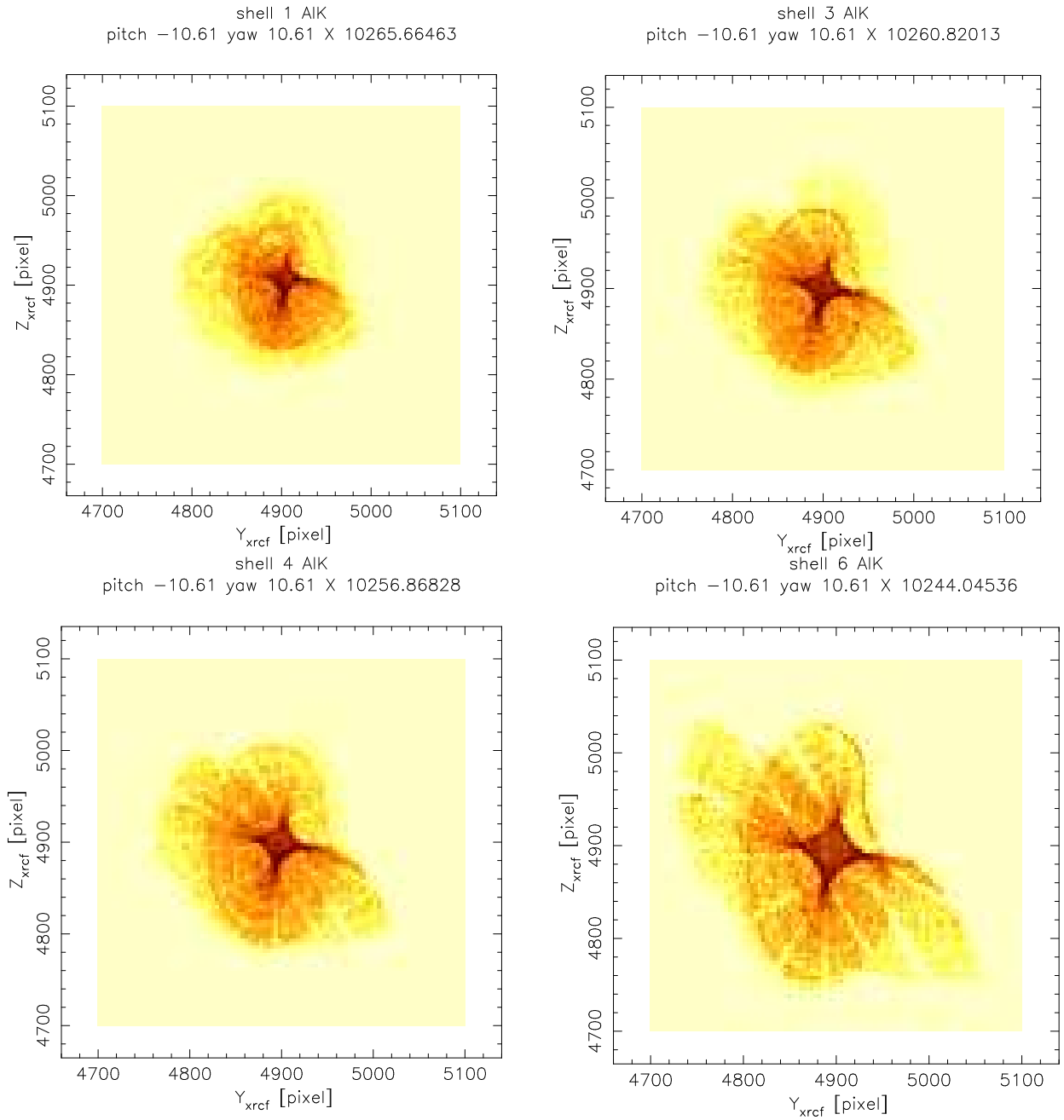

Figure 30.11: Off-axis images for individual shells; pitch = $-10.61'$, yaw = $10.61'$. Pixel width 6.43 μm; binned to 4×4 pixels. Two large overlapping lobes and a dense central pincushion can be seen; the light lanes are shadows of the CAP struts. The concentric ridges in the large lobes result from low-frequency surface errors on the mirrors. (Raytrace data; logarithmic stretch)

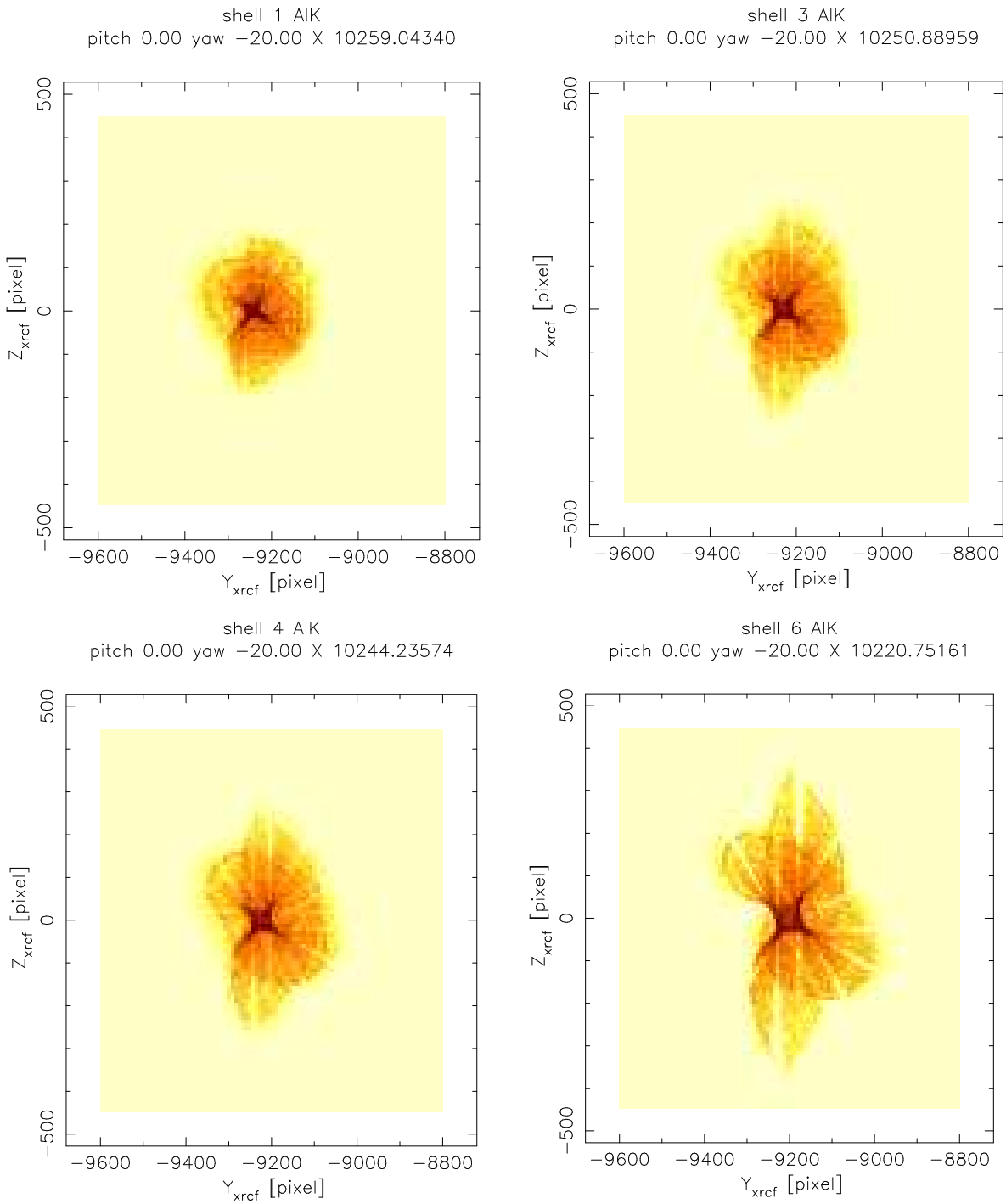

Figure 30.12: Off-axis images for individual shells; pitch = $0'$, yaw = $-20'$. Pixel width $6.43\,\mu$m; binned to 8×8 pixels. Two large overlapping lobes and a dense central pincushion can be seen; the light lanes are shadows of the CAP struts. The concentric ridges in the large lobes result from low-frequency surface errors on the mirrors. (Raytrace data; logarithmic stretch)

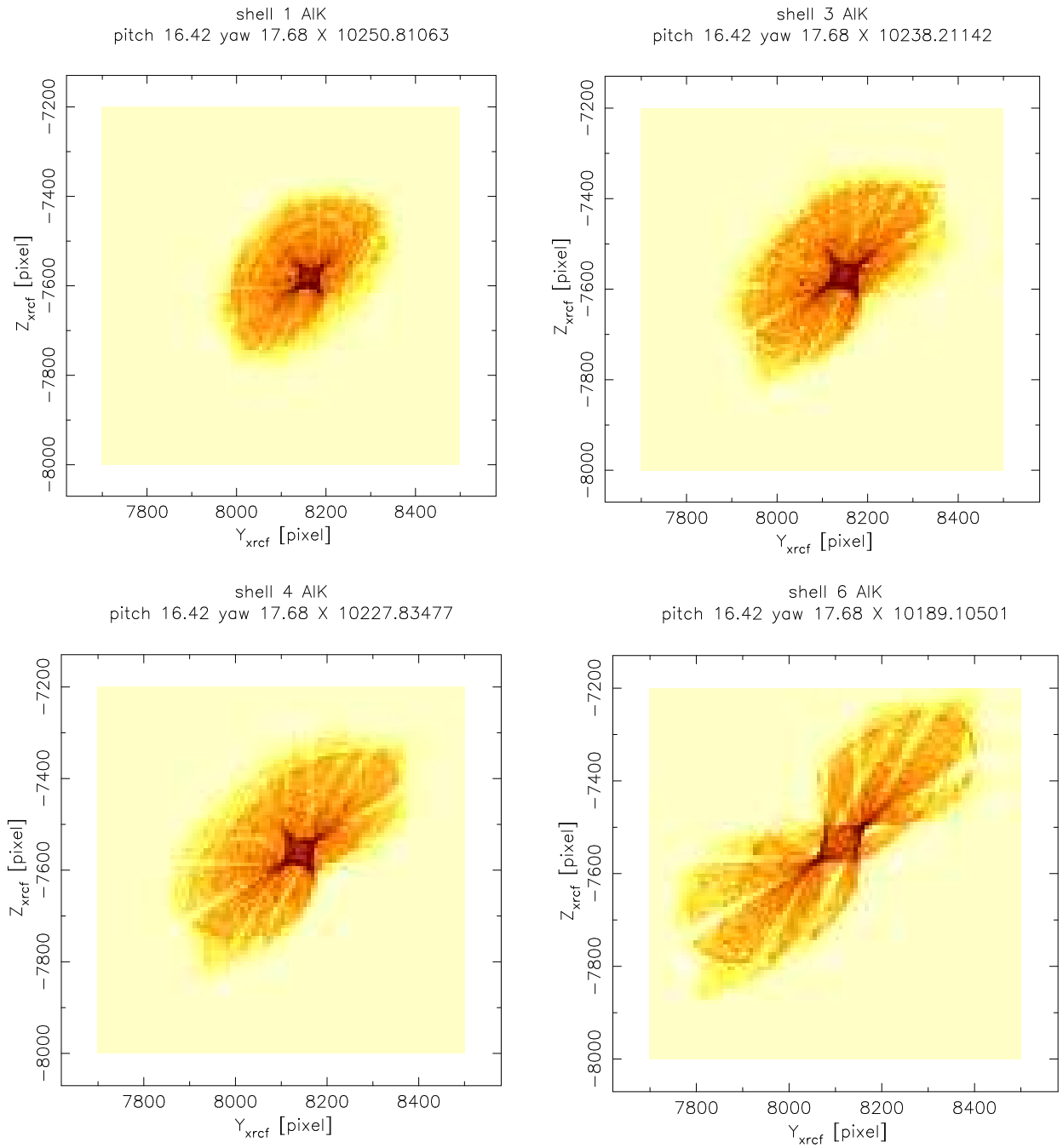

Figure 30.13: Off-axis images for individual shells; pitch = 16.42′, yaw = 17.68′. Pixel width 6.43 μm; binned to 8 × 8 pixels. Two large overlapping lobes and a dense central pincushion can be seen; the light lanes are shadows of the CAP struts. The concentric ridges in the large lobes result from low-frequency surface errors on the mirrors. (Raytrace data; logarithmic stretch)

this will produce a better estimate and allow an assessment of the measurement errors. The model can also be checked against the full-HRMA off-axis images at different energies obtained during Phase 1 of the XRCF testing.

Preliminary raytrace studies show that the HATS Fourier coefficients associated with rigid body alignment are insensitive to a tilt-compensated decenter. The effects may show up in the higher Fourier components but noise in the data may make it impractical to extract a value. Further preliminary studies indicate that a tilt-compensated decenter has little effect on the quadrant shutter focus estimators (of order $10\,\mu$m axially) but could produce a significant bias in the tilt estimates. The analysis in Chapter 28 compared against a model incorporating the estimated tilt-compensated decenter, so whatever bias the decenter introduces is also present in the modeling. Care must be taken, however, in attempting a breakdown into individual components until this bias is better understood.

The effects of the tilt-compensated decenter on the analysis and interpretation of the other calibration data needs to be investigated. Although the tilt-compensated decenter does not produce on-axis coma on-orbit, the finite source distance at XRCF produces an effective spherical aberration which may make the tilt-compensated decenter effects visible in images even on-axis: preliminary raytraces indicate that the on-axis blur circle should be asymmetric. The available on-axis data also needs to be checked to determine whether they are consistent with the measured tilt-compensated decenter values.

The single-shell off-axis images show signs of vignetting by the closed shutters for adjacent shells. It may be possible to ascertain the lateral decenter of the shutter assembly relative to the optical axis by making use of the full set of off-axis images for the individual shells Preliminary raytraces indicate a horizontal decenter by about 2 mm; a further study could refine the decenter of the shutter assembly. Because we have pure yaw cases but not pure pitch cases, it will be easier to constrain the Y_{XRCF} component than the Z_{XRCF} component of the shutter assembly decenter.

Finally, some of the images (single-shell and full HRMA) at large off-axis angles show single-reflection ghost images. Once the tilt-compensated decenters and other alignments of the HRMA are well determined, it may be possible to deduce something about the as-built X-ray baffle placement from the shapes of the off-axis images and the ghost images.